

RelA-Diffusion: Relativistic Adversarial Diffusion for Multi-Tracer PET Synthesis from Multi-Sequence MRI

Minhui Yu, Yongheng Sun, David S. Lalush, Jason P Mihalik, Pew-Thian Yap, Mingxia Liu, *Senior Member, IEEE*



Abstract—Multi-tracer positron emission tomography (PET) provides critical insights into diverse neuropathological processes such as tau accumulation, neuroinflammation, and β -amyloid deposition in the brain, making it indispensable for comprehensive neurological assessment. However, routine acquisition of multi-tracer PET is limited by high costs, radiation exposure, and restricted tracer availability. Recent efforts have explored deep learning approaches for synthesizing PET images from structural MRI. While some methods rely solely on T1-weighted MRI, others incorporate additional sequences such as T2-FLAIR to improve pathological sensitivity. However, existing methods often struggle to capture fine-grained anatomical and pathological details, resulting in artifacts and unrealistic outputs. To this end, we propose RelA-Diffusion, a Relativistic Adversarial Diffusion framework for multi-tracer PET synthesis from multi-sequence MRI. By leveraging both T1-weighted and T2-FLAIR scans as complementary inputs, RelA-Diffusion captures richer structural information to guide image generation. To improve synthesis fidelity, we introduce a gradient-penalized relativistic adversarial loss to the intermediate clean predictions of the diffusion model. This loss compares real and generated images in a relative manner, encouraging the synthesis of more realistic local structures. Both the relativistic formulation and the gradient penalty contribute to stabilizing the training, while adversarial feedback at each diffusion timestep enables consistent refinement throughout the generation process. Extensive experiments on two datasets demonstrate that RelA-Diffusion outperforms existing methods in both visual fidelity and quantitative metrics, highlighting its potential for accurate synthesis of multi-tracer PET.

Index Terms—Brain, Image Synthesis, PET, Structural MRI, Diffusion Model.

1 INTRODUCTION

Accurate assessment and monitoring of neurodegenerative disorders rely heavily on the ability to capture diverse and subtle pathological processes within the brain. Brain positron emission tomography (PET) is a powerful imaging modality that enables the *in vivo* visualization of various molecular targets, including β -amyloid deposition with ^{11}C -PIB (PIB), tau pathology with ^{18}F -AV1451 (TAU) [1]–[4],

and neuroinflammatory activity with ^{18}F -PBR111 (PBR) [5]. This multi-tracer PET imaging can provide complementary information, offering a more comprehensive understanding of disease mechanisms. However, the use of multi-tracer PET imaging in clinical and research settings is hindered by several practical constraints, including high scanning costs, radiation exposure, and limited access to specific tracers. These limitations have motivated the development of alternative approaches that can synthesize PET without requiring tracer administration. Recent research has focused on developing deep learning techniques to synthesize PET images from commonly accessible structural MRI, offering a non-invasive and cost-effective option.

Despite the potential of deep learning for MRI-to-PET synthesis, producing images that are both anatomically precise and pathologically accurate remains a formidable challenge. Earlier GAN-based methods [6]–[11], while capable of generating sharp textures, frequently struggle with optimization instabilities and mode collapse, which can result in the loss of subtle, tracer-specific pathological signatures. Conversely, while more recent diffusion-based strategies [12]–[14] offer superior distribution coverage and training stability, they are prone to producing overly smooth outputs in high-dimensional 3D medical volumes. Most existing frameworks fail to effectively balance the strict anatomical constraints of structural MRI with the high-frequency detail required to represent complex tracer uptake patterns, leading to synthesized results that may lack the fidelity needed for clinical decision-making.

To address these critical limitations, we propose RelA-Diffusion, a novel relativistic adversarial diffusion framework specifically developed to synthesize realistic multi-tracer PET images from multi-sequence MRI scans, including T1-weighted (T1w) and T2-FLAIR (T2F) MR images. As illustrated in Figure 1, RelA-Diffusion employs a conditional denoising diffusion probabilistic model that iteratively transforms Gaussian noise into realistic PET images, conditioned on multi-sequence MRI inputs. To improve training dynamics and enhance image fidelity, we introduce the gradient-penalized relativistic adversarial loss during training. This loss directly compares real and synthesized PET images to encourage sharper anatomical boundaries

M. Yu, Y. Sun, P.-T. Yap and M. Liu are with the Department of Radiology and Biomedical Research Imaging Center (BRIC), University of North Carolina at Chapel Hill, Chapel Hill, NC 27599, USA. M. Yu and D. Lalush are with the Joint Department of Biomedical Engineering, University of North Carolina at Chapel Hill and North Carolina State University, Chapel Hill, NC 27599, USA. J. Mihalik is with the Department of Exercise and Sport Science, UNCH, Chapel Hill, NC 27599, USA.

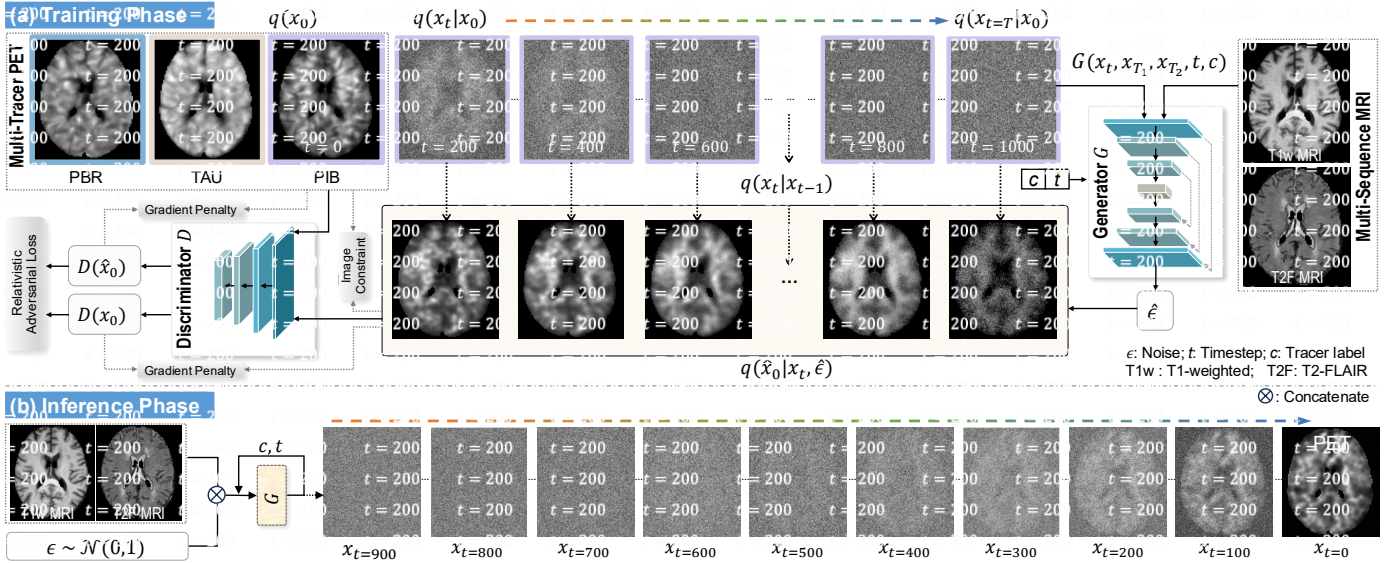


Fig. 1. Illustration of the proposed relativistic adversarial diffusion (RelA-Diffusion) framework that synthesizes multi-tracer PET images from multi-sequence MRI input such as T1-weighted (T1w) and T2-FLAIR (T2F) MRIs.

and more realistic local structures. Both the gradient penalty and the relativistic formulation help stabilize adversarial learning and regularize model behavior, reducing artifacts and promoting detailed structural representation. Extensive evaluations on two multi-tracer PET datasets demonstrate that RelA-Diffusion consistently outperforms state-of-the-art (SOTA) methods in terms of visual realism, anatomical accuracy, and quantitative performance metrics, establishing its effectiveness and reliability for multi-tracer PET image synthesis. The main contributions of this work are summarized as follows:

- We introduce RelA-Diffusion, a diffusion-based framework tailored for multi-tracer PET synthesis from multi-sequence MRI, leveraging both T1-weighted and T2-FLAIR MRI inputs for enhanced pathological sensitivity.
- We propose to apply the gradient-penalized relativistic adversarial feedback to the intermediate clear image estimated during the training of the diffusion model, enabling consistent supervision and improved detail preservation, while stabilizing the training.
- Extensive experiments on two datasets suggest that RelA-Diffusion consistently outperforms existing state-of-the-art methods in visual fidelity and quantitative metrics.

The remainder of this paper is organized as follows. Section 2 reviews the related work. Section 3 introduces the proposed RelA-Diffusion framework, while Section 4 presents the experiments and comparative analysis. In Section 5, we discuss the impact of key components of the proposed method and present the limitations of this study alongside directions for future work. Finally, Section 6 concludes the paper.

2 RELATED WORK

2.1 GAN-based PET Image Synthesis

Earlier methods for MRI-based PET image synthesis primarily employed GAN-based models. Wei *et al.* [6] propose a conditional flexible self-attention GAN model to predict PET parametric maps from multi-sequence MRI, training the GAN using a Sketcher-Refiner approach. Hu *et al.* [7] introduce a bidirectional GAN that learns both PET generation and inversion back to latent representations, aiming to effectively capture semantic content within the latent space. Zhang *et al.* [9] develop BPGAN, which utilizes a 3D multi-convolution U-Net generator with gradient profile and structural similarity index measure constraints to better preserve structural details in synthesized PET images. Several studies have applied CycleGAN-based frameworks for paired MRI-to-PET synthesis. For instance, Pan *et al.* [8] introduce a method that translates between T1-weighted MRI and fluorodeoxyglucose-PET while integrating disease-specific feature disentanglement and diagnosis-guided supervision to enhance clinical relevance. Zhou *et al.* [10] explore translation between multiple PET tracers, conditioning the synthesis process on anatomical context derived from structural MRI. Despite their effectiveness, GAN-based approaches frequently encounter optimization challenges, such as mode collapse, which can significantly limit model performance [15].

2.2 Diffusion Models for Medical Imaging

More recent strategies have shifted toward diffusion models, which offer significant advantages in generating high-quality medical images. For example, a Joint Diffusion Attention Model (JDAM) [12] is designed to generate synthetic PET images from high-field and ultra-high-field MRI by learning the joint probability distribution between MRI input and the noisy PET output. Another study [13] presents a functional imaging constrained diffusion (FICD) method, incorporating a voxel-wise alignment loss to improve the

quantitative fidelity of PET predictions by enforcing agreement with the ground truth. Additionally, a diffusion model MTGD [14] is designed to fuse multi-sequence MRI to facilitate multi-tracer PET synthesis, showing improved performance in combining complementary MRI contrasts.

To leverage the strengths of both paradigms, several approaches have integrated GAN objectives into diffusion frameworks. The study by [16] models each denoising step of a diffusion process using a multi-modal conditional GAN, allowing for significantly faster sampling while maintaining high sample quality and diversity, and improving mode coverage and training stability compared to traditional GANs. Another study [17] introduces Diffusion-GAN, a GAN framework that injects instance noise generated by a forward diffusion chain into the discriminator’s input, thereby addressing GAN training instability and mode collapse by providing more stable and diverse learning signals. While these hybrid frameworks mitigate several limitations of standalone GANs and diffusion models, they often introduce complex training dynamics due to the competing nature of adversarial and denoising objectives. Consequently, such models may struggle to balance global structural coherence with fine-grained detail, leading to suboptimal synthesis fidelity in some cases, a significant challenge that our RelA-Diffusion framework aims to solve.

3 PROPOSED METHOD

We propose **RelA-Diffusion**, a conditional diffusion framework for synthesizing high-fidelity multi-tracer PET images from multi-sequence MRI. Figure 1 shows that RelA-Diffusion introduces a stabilized adversarial supervision mechanism to diffusion training by leveraging a gradient-penalized relativistic discriminator to provide feedback on intermediate clean predictions \hat{x}_0 at each training step. This feedback guides the learning of fine-grained tracer uptake patterns while promoting stable optimization dynamics throughout denoising process.

3.1 Overall Framework

RelA-Diffusion consists of two main components: a *conditional denoising diffusion model* as the generator G , and a *relativistic discriminator* D used only during training. As illustrated in Figure 1, the generator predicts the noise component $\hat{\epsilon} = G(x_t, x_{T_1}, x_{T_2}, t, c)$ at each denoising step t , where x_t is the noisy image, x_{T_1} and x_{T_2} are the T1w and T2F MRI inputs, and c denotes the tracer label. The clean image estimate \hat{x}_0 is then computed from the predicted noise and x_t using the DDPM formulation [18]. The discriminator $D(\hat{x}_0, x_0)$ compares the predicted \hat{x}_0 with the ground-truth PET image x_0 in a relativistic manner to provide adversarial feedback on the relative realism of the intermediate prediction. At inference time, only the trained generator G is used to synthesize PET images through the learned reverse diffusion process, without involving the discriminator.

Our generative model follows a conditional denoising diffusion framework [18], which defines a forward noising process as a fixed Markov chain that progressively corrupts a clean PET image x_0 into a sequence of noisy variables

$\{x_t\}_{t=1}^T$ over T timesteps. This is achieved by adding Gaussian noise at each step according to a predefined noise schedule [18]. The reverse denoising process is then learned to invert this degradation, reconstructing the original data by estimating the noise added at each step.

3.1.1 Forward Diffusion Process

Given a real PET image $x_0 \sim q(x_0)$, the forward process adds Gaussian noise over T timesteps, creating a series of noisy samples $\{x_1, \dots, x_T\}$. This process is defined by a fixed Markov chain:

$$q(x_{1:T}|x_0) = \prod_{t=1}^T q(x_t|x_{t-1}), \quad (1)$$

$$q(x_t|x_{t-1}) = \mathcal{N}(x_t; \sqrt{1 - \beta_t}x_{t-1}, \beta_t \mathbf{I}), \quad (2)$$

where \mathcal{N} is Gaussian distribution with mean μ_t and variance σ_t , β_t is a time-dependent hyperparameter that controls the noise level at each timestep, and \mathbf{I} is the identity matrix indicating isotropic variance. The marginal distribution at timestep t can be expressed as:

$$q(x_t|x_0) = \mathcal{N}(x_t; \sqrt{\bar{\alpha}_t}x_0, (1 - \bar{\alpha}_t)\mathbf{I}), \quad (3)$$

where $\alpha_t = 1 - \beta_t$ and $\bar{\alpha}_t = \prod_{s=1}^t \alpha_s$.

3.1.2 Reverse Denoising Process

Starting from a noisy image x_t , the reverse denoising process aims to progressively estimate and remove noise to recover the cleaner image x_{t-1} in the previous timestep, and ultimately aims to reconstruct the original data x_0 . The trainable component for this process is a generator G that predicts the noise ϵ added to x_0 during the forward diffusion process to obtain x_t , denoted as $\hat{\epsilon}$. As illustrated in the top right of Figure 1, the generator is conditioned on multi-sequence MRI inputs (i.e., x_{T_1} for T1w MRI and x_{T_2} for T2F MRI) via input channel concatenation, and conditioned on the tracer label c and timestep t via cross-attention mechanisms, allowing the model to leverage anatomical information from MRI and the target tracer type to guide PET image synthesis.

In the *training phase*, a randomly selected timestep $t \in \{1, \dots, T\}$ is sampled uniformly, and a noisy image x_t is generated by adding Gaussian noise to the ground-truth PET image x_0 according to the forward diffusion process:

$$x_t = \sqrt{\bar{\alpha}_t}x_0 + \sqrt{1 - \bar{\alpha}_t}\epsilon, \quad \epsilon \sim \mathcal{N}(0, \mathbf{I}). \quad (4)$$

The generator G is then trained to predict the added noise ϵ from the noisy image x_t . The training objective is to minimize the mean squared error (MSE) between the predicted noise $\hat{\epsilon}$ and the ground-truth noise ϵ , defined as:

$$\mathcal{L}_N = \frac{1}{n} \sum_{i=1}^n (\epsilon - \hat{\epsilon}(x_t, t, x_{T_1}, x_{T_2}))^2, \quad (5)$$

where n denotes the number of samples. Given this predicted noise, an estimate of the clean image \hat{x}_0 at timestep t can be computed as:

$$\hat{x}_0(x_t, t) = \frac{x_t - \sqrt{1 - \bar{\alpha}_t}\hat{\epsilon}}{\sqrt{\bar{\alpha}_t}}. \quad (6)$$

In the *inference phase*, the generator iteratively applies its noise predictions to progressively denoise an initial pure

Gaussian noise input, starting from x_T and moving step-by-step towards x_0 . At each step, the generator predicts the noise $\hat{\epsilon}$, which is then utilized to estimate a cleaner version:

$$x_{t-1} = \frac{1}{\sqrt{\alpha_t}} \left(x_t - \frac{1 - \alpha_t}{\sqrt{1 - \bar{\alpha}_t}} \hat{\epsilon} \right) + \sigma_t z, \quad (7)$$

where σ_t is the standard deviation of added noise and $z \sim \mathcal{N}(0, 1)$. This iterative sampling procedure, guided by the estimated \hat{x}_0 and the conditional multi-sequence MRI and tracer label inputs, generates the multi-tracer PET image.

3.2 Supervision on Intermediate Clean Predictions

To enhance output fidelity, we introduce the following two constraints on the intermediate clean image \hat{x}_0 by comparing them against the true x_0 in RelA-Diffusion.

3.2.1 Image Constraint

The image-level constraint aims to minimize the l_1 loss between \hat{x}_0 and x_0 , formulated as:

$$\mathcal{L}_I = \frac{1}{n} \sum_{i=1}^n |x_0 - \hat{x}_0|, \quad (8)$$

where n is the number of samples in the training batch. This design explicitly guides \hat{x}_0 during training to promote more reliable outputs across the entire reverse process. It is essential since denoising becomes increasingly difficult at larger timesteps, where the input x_t is heavily corrupted. Supervising \hat{x}_0 at all timesteps implicitly places stronger regularization on the model’s behavior in high-noise diffusion steps, enabling the network to recover meaningful details even from severely degraded inputs. This effect has been theoretically discussed in prior works [13], [19] and provides a foundation for the subsequent adversarial feedback, ensuring that the discriminator receives informative and reliable intermediate predictions at all diffusion steps.

3.2.2 Gradient-Penalized Relativistic Adversarial Constraint

To further enhance realism of synthesized PET images, we integrate a *relativistic adversarial loss* [20], [21]. Unlike traditional GANs where the discriminator judges whether an image is real or fake in an absolute manner, a relativistic discriminator assesses whether a generated image is more realistic than a real image, or vice versa. The discriminator D is a classifier that receives both intermediate clean predictions \hat{x}_0 produced from noisy PET and the corresponding real PET image x_0 . We perform pairwise comparison to estimate the relative authenticity between real and generated samples. Denote \mathbb{P} and \mathbb{Q} as the probability distributions of real and synthesized PET images, respectively. The relativistic adversarial (RA) loss is formulated as:

$$\mathcal{L}_R = \mathbb{E}_{(x_0, \hat{x}_0) \sim (\mathbb{P}, \mathbb{Q})} [f(D(\hat{x}_0) - D(x_0))] + \mathbb{E}_{(x_0, \hat{x}_0) \sim (\mathbb{P}, \mathbb{Q})} [f(D(x_0) - D(\hat{x}_0))], \quad (9)$$

where $D(x)$ denotes the discriminator’s scalar output for image x , $D(\hat{x})$ denotes the output for the synthesized image \hat{x} , $f(y) = -\log(1 + e^{-y})$ is the activation function [22], and the expectations are computed over the batch of real and synthesized images. The first term in Eq. (9) encourages the generator to increase the relative realism of its outputs

compared to real PET images. The second term is designed to estimate how much more realistic a real image is compared to a generated one, rather than assigning a realism score to each image in isolation. Compared to conventional GANs, which can suffer from gradient saturation and mode collapse due to the discriminator’s binary real/fake decisions, the relativistic mechanism has been shown to provide a smoother learning signal that stabilizes adversarial training. It can also improve image quality by preventing the discriminator from becoming overly confident in real-vs-fake discrimination, to maintain meaningful gradients throughout training. Applied jointly with the diffusion loss, it promotes more consistent improvements in the perceptual quality of the diffusion model and guides the model toward producing more realistic outputs.

To facilitate model training, we also incorporate a zero-centered *gradient penalty* on both real and generated data [21]. Specifically, we penalize the squared norm of the discriminator’s gradients with respect to its inputs. This penalty constrains the gradient norm of the discriminator D on the real PET image x_0 and the generated image \hat{x}_0 , which is formulated as:

$$\mathcal{L}_G = \mathbb{E}_{x_0 \sim \mathbb{P}} [\|\nabla_{x_0} D(x_0)\|^2] + \mathbb{E}_{\hat{x}_0 \sim \mathbb{Q}} [\|\nabla_{\hat{x}_0} D(\hat{x}_0)\|^2], \quad (10)$$

where ∇ is the gradient operation. This gradient penalty (GP) is designed to promote smoother discriminator behavior on both real and synthesized PET images, improving convergence and ensuring stability throughout training [21], [23].

3.2.3 Overall Training Objective

The RelA-Diffusion framework is trained by minimizing a hybrid objective function that balances the diffusion model’s noise prediction accuracy with the image constraint and the gradient-penalized adversarial guidance for realism. The hybrid loss is formulated as:

$$\mathcal{L} = \mathcal{L}_N + \mathcal{L}_I + \mathcal{L}_R + \mathcal{L}_G. \quad (11)$$

3.3 Implementation

The *generator* is implemented using a U-Net architecture, consisting of 3 downsampling and 3 upsampling blocks. Each downsampling block contains one convolutional layer for spatial reduction and two residual sub-blocks incorporating skip connections. Each residual sub-block consists of two convolutional layers, each followed by group normalization and timestep embedding, along with a shortcut connection. Positional embeddings for the diffusion timestep t plus tracer label c project encoded features to match the number of feature channels, enabling effective feature integration. The multi-sequence MRI inputs are concatenated along the channel dimension and then fed into U-Net along with the input x_t . The *discriminator* is based on a PatchGAN discriminator architecture [24], designed to operate on local image patches rather than the entire image. It consists of 3 convolutional layers with decreasing spatial resolution and increasing channel depth. Each convolutional layer is followed by LeakyReLU activation (with a negative slope of 0.2) and batch normalization, except for the final output

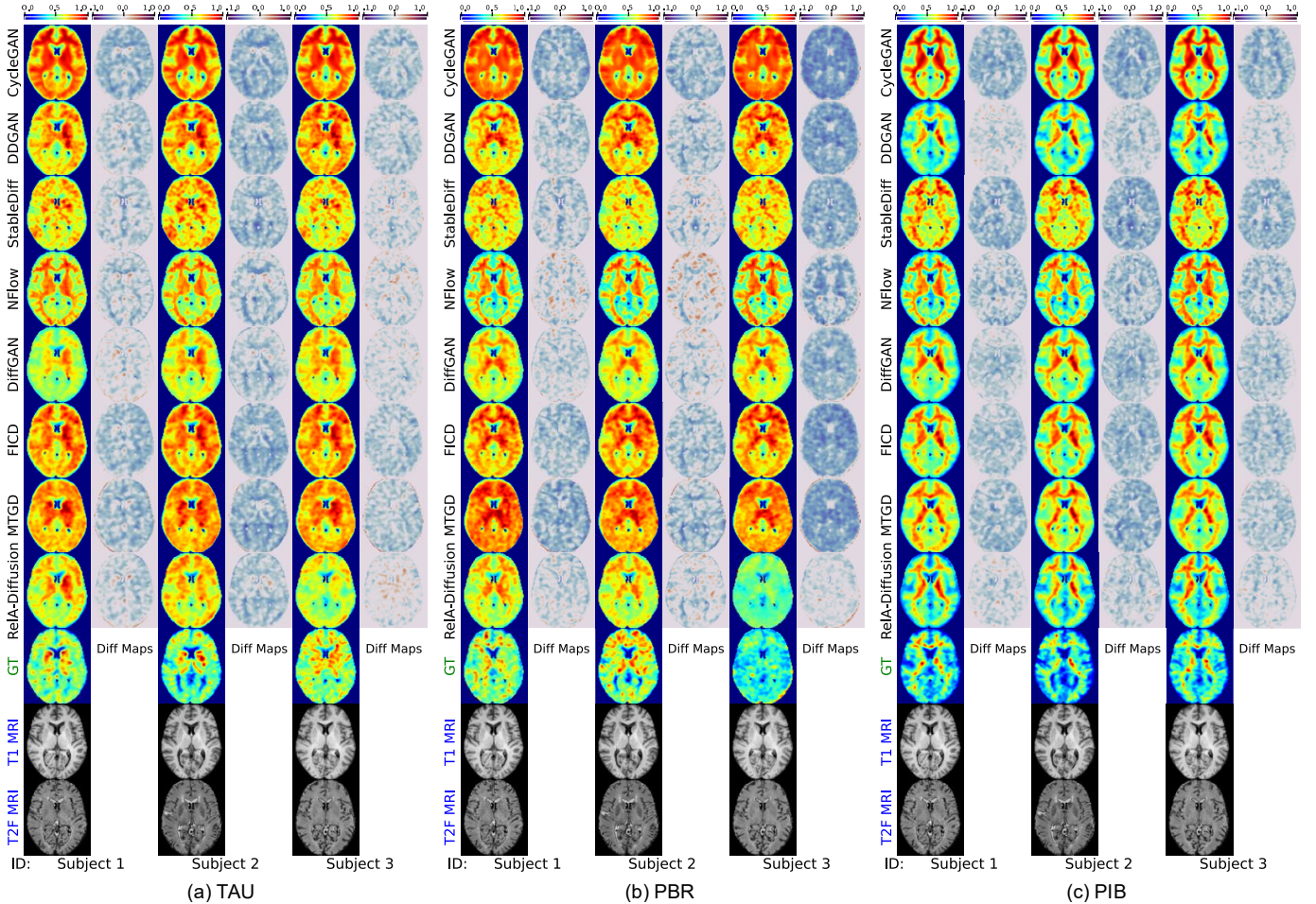


Fig. 2. Visualization of test PET images for (a) TAU, (b) PBR, and (c) PIB, synthesized by 8 methods, along with corresponding difference (Diff) maps. Ground-truth (GT) and input T1w/T2F MRIs with subject IDs are shown at the bottom.

TABLE 1

Quantitative results of eight methods for TAU-, PBR- and PIB-PET generation on NFL-LONG (best results in bold). The column *Sig.* indicates statistically significant ($p < 0.05$) via t -test on SSIM.

Method	Synthesized TAU-PET Image				Synthesized PBR-PET Image				Synthesized PIB-PET Image			
	PSNR \uparrow	SSIM \uparrow	MAE \downarrow	Sig.	PSNR \uparrow	SSIM \uparrow	MAE \downarrow	Sig.	PSNR \uparrow	SSIM \uparrow	MAE \downarrow	Sig.
CycleGAN [10]	27.506 \pm 1.598	0.869 \pm 0.013	0.017 \pm 0.004	*	28.065 \pm 2.687	0.833 \pm 0.022	0.017 \pm 0.007	*	24.954 \pm 2.274	0.846 \pm 0.017	0.024 \pm 0.010	*
DDGAN [16]	25.448 \pm 2.373	0.892 \pm 0.015	0.025 \pm 0.009	*	25.201 \pm 3.044	0.884 \pm 0.017	0.027 \pm 0.011	*	26.382 \pm 2.561	0.870 \pm 0.018	0.021 \pm 0.010	*
StableDiff [26]	26.483 \pm 4.426	0.881 \pm 0.031	0.023 \pm 0.015	*	28.845 \pm 2.681	0.892 \pm 0.019	0.015 \pm 0.006	*	25.245 \pm 1.735	0.852 \pm 0.013	0.023 \pm 0.007	*
NFlow [27]	27.615 \pm 3.490	0.881 \pm 0.020	0.019 \pm 0.010	*	28.844 \pm 2.030	0.887 \pm 0.013	0.015 \pm 0.004	*	24.522 \pm 1.304	0.805 \pm 0.017	0.024 \pm 0.004	*
DiffGAN [17]	24.980 \pm 2.330	0.884 \pm 0.013	0.026 \pm 0.009	*	23.112 \pm 2.938	0.870 \pm 0.021	0.034 \pm 0.012	*	23.491 \pm 2.640	0.855 \pm 0.021	0.031 \pm 0.013	*
FICD [13]	24.236 \pm 2.877	0.883 \pm 0.015	0.030 \pm 0.012	*	25.594 \pm 2.945	0.885 \pm 0.017	0.025 \pm 0.010	*	24.229 \pm 2.860	0.860 \pm 0.021	0.029 \pm 0.012	*
MTGD [14]	24.998 \pm 1.937	0.872 \pm 0.012	0.026 \pm 0.008	*	23.847 \pm 2.379	0.859 \pm 0.012	0.031 \pm 0.010	*	25.677 \pm 2.326	0.846 \pm 0.013	0.023 \pm 0.010	*
RelA-Diffusion (Ours)	28.314 \pm 3.392	0.898 \pm 0.017	0.017 \pm 0.009	—	29.324 \pm 2.437	0.898 \pm 0.017	0.015 \pm 0.006	—	26.270 \pm 1.687	0.861 \pm 0.012	0.020 \pm 0.006	—

A latent diffusion model that encodes 3D images into a compact latent space before applying diffusion-based modality translation, and then uses a decoder to recover the image from the latent space. Its encoder and decoder components are pretrained on all training PET images in this study and kept frozen during the diffusion model’s training for the modality translation task. (4) Normalizing Flow (NFlow) [27]: A normalizing flow-based model trained end-to-end, leveraging normalizing flows to guide PET synthesis. (5) Diffusion GAN (DiffGAN) [17]: This GAN framework injects instance noise, generated by a forward diffusion chain, into the discriminator’s input. This approach aims to address GAN training instability and mode collapse

by providing more stable and diverse learning signals. (6) FICD [13]: A denoising diffusion probabilistic model that learns a reverse denoising process within a Markov chain and constrained by the clear intermediate prediction. (7) MTGD [14]: A diffusion-based model for multi-tracer PET synthesis from multi-sequence MRI (T1w, T2w, T2F), using a Multi-Sequence Attention Encoder and cross-attention fusion. The fused representation, combined with timestep and tracer label, conditions the U-Net via its bottleneck. To ensure a fair comparison, all methods are implemented on 3D images, with architectures and hyperparameters kept as consistent as possible. All diffusion models operate at the image level (i.e., FICD, DDGAN, DiffGAN, and MTGD)

implement the image constraint \mathcal{L}_I supervision on intermediate clean predictions as standard DDPM often fails to capture fine structural details in 3D settings. Diffusion models (i.e., DDGAN, StableDiff, DiffGAN, FICD, and MTGD) receive input by concatenating T1w and T2F MRI and noisy PET along the channel dimension, and synthesize tracer-specific PET based on the input label. The tracer label is embedded together with the diffusion timestep and injected into the network. CycleGAN and NFlow input concatenated T1w and T2F MRI and generate three-channel outputs, each representing a tracer-specific PET image.

4.2 Result and Analysis

4.2.1 Qualitative Results

Figure 2 displays axial PET slices synthesized by RelA-Diffusion and seven competing methods on the NFL-LONG dataset, alongside the corresponding ground-truth PET images and input T1w and T2F MRIs shown at the bottom. For each method, we also visualize difference (Diff) maps between its synthesized PET and the ground truth to highlight voxel-level deviations. As shown in Figure 2, RelA-Diffusion consistently produces PET images with higher visual quality and closer resemblance to the ground truth compared to the competing approaches. This improvement is particularly evident in PBR and PIB tracers, where our method effectively captures subject-specific patterns of neuroinflammation and amyloid deposition in the brain. In contrast, the competing methods tend to generate similar outputs across different subjects, failing to reflect individual biological variation. Hybrid methods that combine diffusion with adversarial learning (e.g., DiffGAN and RelA-Diffusion) outperform those relying solely on GANs (CycleGAN) or diffusion models (FICD, MTGD, StableDiff). This demonstrates the advantage of incorporating adversarial supervision into diffusion frameworks for improved PET image synthesis.

4.2.2 Quantitative Results

Table 1 summarizes the quantitative performance of all methods on NFL-LONG. Across all three tracers, RelA-Diffusion consistently achieves the best or highly competitive results. For TAU-PET synthesis, it achieves the highest PSNR (28.314) and SSIM (0.898), and ties with CycleGAN for the lowest MAE (0.017), indicating accurate voxel-wise reconstruction and strong anatomical preservation. For PBR-PET, RelA-Diffusion again achieves the best performance with a PSNR of 29.324, SSIM of 0.898, and MAE of 0.015, outperforming StableDiff and NFlow. Although the latter obtain competitive MAE values, their lower PSNR and SSIM suggest that RelA-Diffusion more faithfully preserves tracer patterns. For PIB-PET synthesis, while DDGAN obtains the highest SSIM (0.870), RelA-Diffusion still delivers the best MAE (0.020) and a competitive PSNR (26.270), outperforming other diffusion-based methods (FICD and MTGD).

4.2.3 Region-Level Evaluation Results

Beyond whole-image analysis, we perform region-level evaluation to assess tracer quantification across five standardized CenTauR volumes-of-interest (VOIs) [30], comparing synthesized and ground-truth TAU-PET. As shown in

Figure 4 (a), RelA-Diffusion demonstrates superior consistency between predicted and ground-truth VOI mean SUVr values compared to all competing methods. Our method achieves the tightest clustering along the identity line across all regions, including Universal, Frontal, Mesial Temporal, Meta Temporal, and Temporo-Parietal VOIs. Quantitatively, RelA-Diffusion consistently yields the lowest MAE and root mean square error (RMSE) in every region, including those highly sensitive to early tau accumulation (e.g., Temporal VOIs). In Figure 4 (b), we evaluate the structural integrity of synthesized images using masked SSIM across five VOIs. RelA-Diffusion demonstrates superior structural fidelity compared to all competing methods, maintaining high consistency particularly in the Frontal (SSIM: 0.8582) and Mesial Temporal (SSIM: 0.8678) regions. While competing methods show significant performance degradation in these tau-sensitive areas (with some dropping below 0.50), our framework remains robust across all regions, consistently outperforming these SOTA approaches.

5 DISCUSSION

In this study, we present RelA-Diffusion, a novel relativistic adversarial diffusion framework designed for high-fidelity multi-tracer PET synthesis from multi-sequence MRI. By integrating a gradient-penalized relativistic adversarial loss into the reverse diffusion process, our method effectively balances the preservation of global anatomical structures with the generation of fine-grained, tracer-specific pathological details. Our experimental results on the NFL-LONG and the ADNI cohorts demonstrate that RelA-Diffusion significantly outperforms SOTA GAN and diffusion-based approaches in terms of visual fidelity and quantitative accuracy. The following sections evaluate the robustness of our model through external generalization, assess its clinical utility in downstream cognitive tasks, and explore the computational efficiency of its latent-space extension. Finally, we provide an ablation study to validate the contribution of each framework component and discuss current limitations alongside directions for future work.

5.1 Generalization to External Data

5.1.1 Quantitative and Qualitative Evaluation

To assess the generalization capability of our method, we perform external evaluation on ADNI [29], which includes paired T1w and T2F MRIs along with TAU-PET scans acquired using the AV1451 tracer. Without any fine-tuning, the model trained on NFL-LONG is directly applied to 30 ADNI subjects for TAU-PET synthesis. Table 2 and Figure 3 present the qualitative examples and quantitative metrics for multi-sequence MRI to TAU-PET synthesis on ADNI.

As shown in Table 2, our method consistently achieves the best performance across all metrics when compared with the seven SOTA methods, demonstrating superior generalization capability. Diffusion-only methods (e.g., FICD and MTGD) cannot yield good results compared to hybrid approaches such as DiffGAN, suggesting limited generalizability to unseen data. The qualitative results in Figure 3 further support this observation, where RelA-Diffusion produces images that closely resemble the ground truth, and

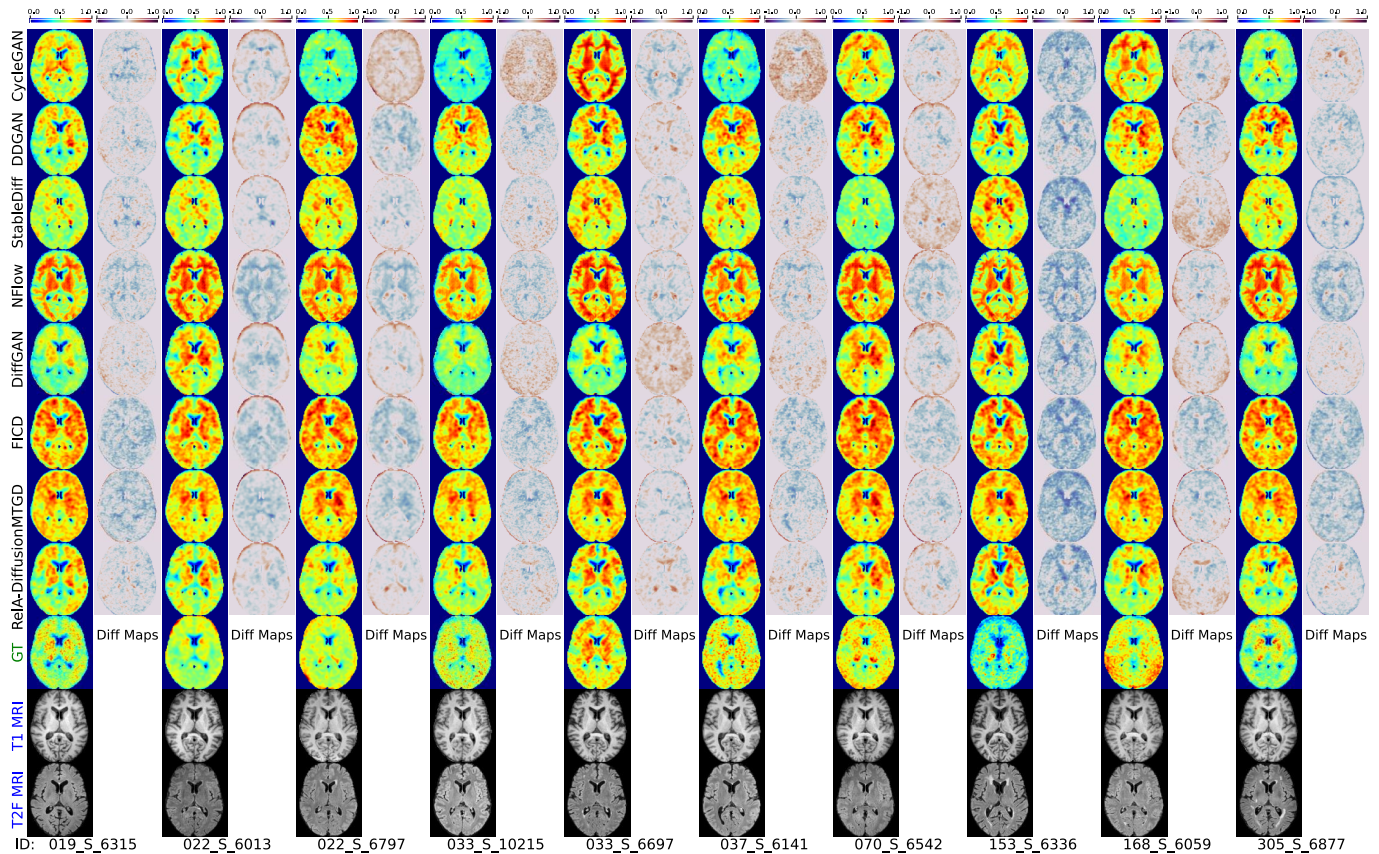


Fig. 3. Visualization of test ADNI TAU-PET images synthesized by 8 methods, and difference (Diff) maps. The ground-truth (GT) PET images along with the input T1w and T2F MRIs are displayed at the bottom with the corresponding subject IDs.

TABLE 2
Quantitative results of eight methods for synthesized ADNI TAU-PET images (best results in bold).

Method	PSNR \uparrow	SSIM \uparrow	MAE \downarrow
CycleGAN [10]	23.766 \pm 3.170	0.843 \pm 0.034	0.030 \pm 0.015
DDGAN [16]	20.563 \pm 3.126	0.839 \pm 0.028	0.045 \pm 0.018
StableDiff [26]	22.179 \pm 3.279	0.838 \pm 0.035	0.038 \pm 0.018
NFlow [27]	25.449 \pm 2.635	0.851 \pm 0.033	0.024 \pm 0.010
DiffGAN [17]	24.797 \pm 2.887	0.862 \pm 0.029	0.026 \pm 0.011
FICD [13]	18.624 \pm 2.934	0.831 \pm 0.028	0.058 \pm 0.021
MTGD [14]	17.632 \pm 2.374	0.818 \pm 0.023	0.064 \pm 0.019
RelA-Diffusion (Ours)	23.781 \pm 3.993	0.864 \pm 0.034	0.032 \pm 0.015

the corresponding difference (Diff) maps are visibly lighter. These findings highlight the strong generalizability of our method when applied to external datasets acquired from different scanners and scanning protocols, suggesting its greater potential for clinical deployment across diverse imaging environments.

5.1.2 Evaluation on Downstream Tasks

To evaluate the clinical utility of synthesized PET images, we conduct downstream regression tasks to predict age, Mini-Mental State Examination (MMSE), and Montreal Cognitive Assessment (MoCA) scores on external ADNI data. We compare two input settings: (1) using MRI only, and (2) using MRI combined with synthesized PET (syn-PET) generated from ADNI TAU-PET images. All regression models share the same ResNet-based architecture [31] and training protocol to ensure a fair comparison. Results in

Fig. 5 reveal that, while structural MRI provides a baseline for cognitive score prediction, integrating synthetic PET leads to a marked reduction in prediction error and tighter correlation coefficients (CC) across age, MMSE, and MoCA tasks. This performance gain suggests that RelA-Diffusion effectively captures latent tau-pathology signatures (such as the topographic distribution of neurofibrillary tangles) that are not yet manifested as macroscopic cortical thinning in T1w or T2F sequences. Specifically, for MoCA and MMSE prediction tasks, which rely on localized cortical integrity, the syn-PET likely provides a surrogate for metabolic decline that precedes the macroscopic structural atrophy captured by MRI. These results indicate that the synthesized images preserve clinically relevant functional information.

5.2 Latent Extension of RelA-Diffusion

We further develop a latent-space variant of our framework, termed RelA-Diffusion-Latent, to improve computational efficiency. Instead of directly operating in the voxel space, both conditional MRI inputs and target PET images are first encoded into a latent space ($10 \times 12 \times 10$) using a pretrained frozen autoencoder. The diffusion model operates entirely in this latent space. The diffusion processes and the relativistic adversarial supervision remain the same as RelA-Diffusion. We apply the image constraint L_I directly on the predicted clean latent \hat{z}_0 to enforce accurate reconstruction in the latent domain. The gradient-penalized relativistic adversarial constraint is applied on the *decoded* PET image \hat{x}_0 , obtained

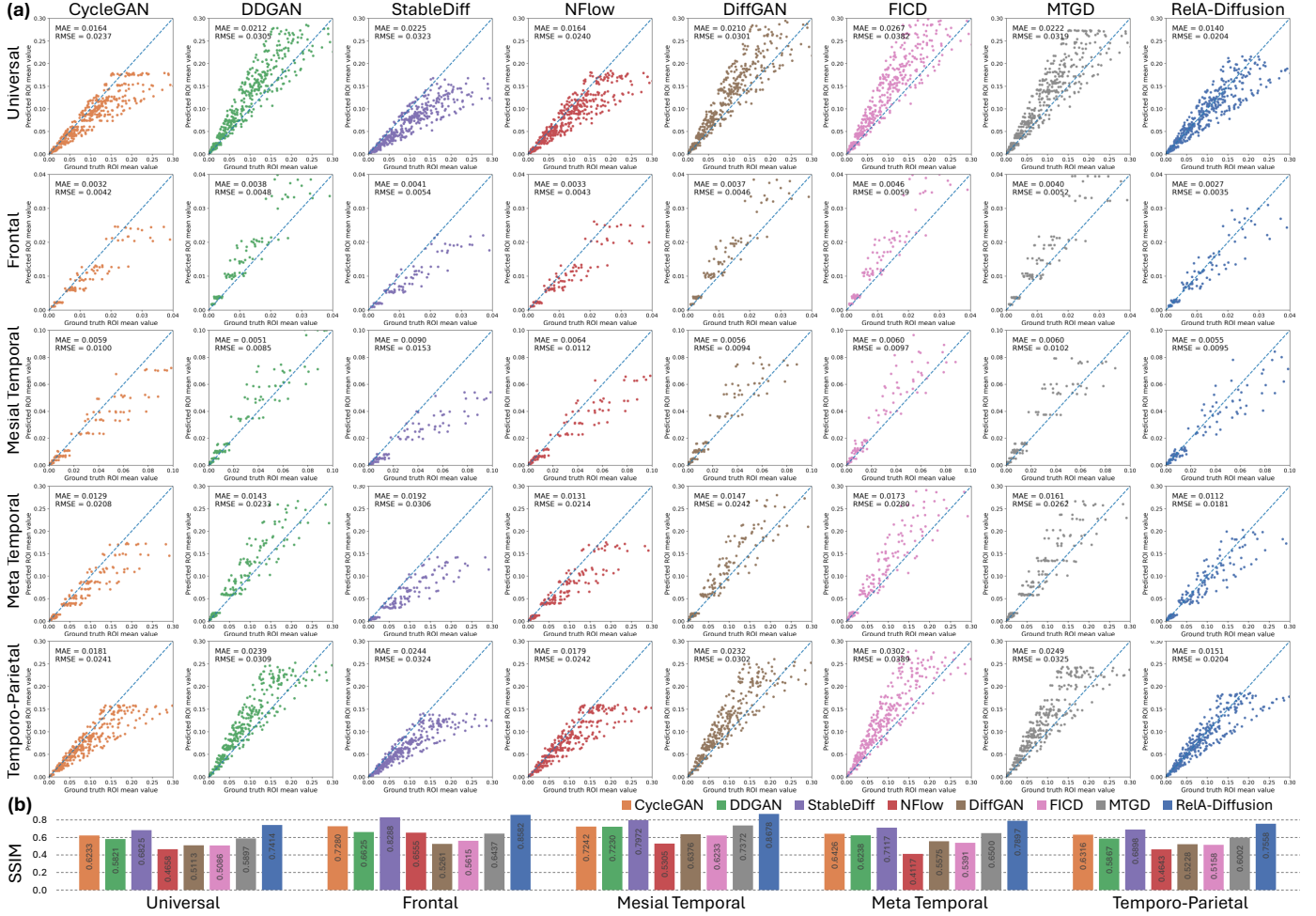


Fig. 4. Region-level quantitative evaluation on NFL-LONG. (a) Scatter plots of predicted vs. ground-truth volume-of-interest (VOI) mean SUVr for TAU-PET across eight methods and five tau-related VOIs (Frontal, Mesial Temporal, Meta Temporal, Temporo-Parietal, and Universal) [30], with MAE and RMSE reported in each panel. (b) Comparison of SSIM results across the same five VOIs [30].

TABLE 3

Quantitative results achieved by RelA-Diffusion, as well as their degraded variants for multi-tracer PET generation on NFL-LONG, with best results shown in bold.

Method	Synthesized TAU-PET Image			Synthesized PBR-PET Image			Synthesized PIB-PET Image		
	PSNR \uparrow	SSIM \uparrow	MAE \downarrow	PSNR \uparrow	SSIM \uparrow	MAE \downarrow	PSNR \uparrow	SSIM \uparrow	MAE \downarrow
w/oRA	28.156 \pm 4.304	0.908 \pm 0.023	0.019 \pm 0.012	29.311 \pm 2.547	0.912 \pm 0.018	0.015 \pm 0.006	25.408 \pm 2.182	0.877 \pm 0.010	0.022 \pm 0.006
w/oGP	18.401 \pm 2.780	0.780 \pm 0.027	0.061 \pm 0.021	20.947 \pm 2.732	0.786 \pm 0.029	0.045 \pm 0.013	16.855 \pm 0.953	0.764 \pm 0.008	0.066 \pm 0.007
w/oRAGP	24.956 \pm 4.644	0.877 \pm 0.038	0.029 \pm 0.016	29.261 \pm 4.173	0.900 \pm 0.029	0.016 \pm 0.010	23.721 \pm 3.166	0.850 \pm 0.020	0.029 \pm 0.010
w/oT2F	28.109 \pm 4.457	0.898 \pm 0.029	0.019 \pm 0.013	29.490 \pm 2.380	0.905 \pm 0.017	0.014 \pm 0.005	25.366 \pm 1.814	0.863 \pm 0.012	0.022 \pm 0.005
w/oT1w	26.022 \pm 4.721	0.887 \pm 0.035	0.026 \pm 0.016	29.894 \pm 2.839	0.907 \pm 0.020	0.014 \pm 0.006	23.695 \pm 2.748	0.851 \pm 0.014	0.029 \pm 0.008
RelA-Diffusion	28.314 \pm 3.392	0.898 \pm 0.017	0.017 \pm 0.009	29.324 \pm 2.437	0.898 \pm 0.017	0.015 \pm 0.006	26.270 \pm 1.687	0.861 \pm 0.012	0.020 \pm 0.006

by passing \hat{z}_0 through the decoder, allowing the discriminator to assess perceptual realism in image space. This hybrid latent-image supervision strategy preserves the computational advantages of latent diffusion while retaining strong adversarial guidance for high-fidelity PET synthesis. Table 4 compares RelA-Diffusion and RelA-Diffusion-Latent, showing comparable synthesis performance while the latent version significantly reduces inference time. RelA-Diffusion-Latent achieves an inference speed of 0.778 s/vol, which is even faster than the GAN baseline (CycleGAN: 1.47 s/vol), while diffusion-only methods such as FICD remain much slower (134.8 s/vol). This suggests that the latent variant achieves an excellent balance between efficiency and fidelity.

5.3 Ablation Study

To evaluate the contributions of key components in our RelA-Diffusion framework, we conduct an ablation study on NFL-LONG by comparing it to four ablated variants: (1) **w/oRA**, which replaces the relativistic adversarial loss with a standard non-relativistic GAN loss; (2) **w/oGP**, which removes gradient penalties; (3) **w/oRAGP**, which replaces the relativistic adversarial loss with a standard non-relativistic GAN loss and removes gradient penalties; (4) **w/oT2F**, which excludes T2F input and uses only T1w MRI as condition; and (5) **w/oT1w**, which uses only T2F MRI and

TABLE 4
Quantitative results and inference time of RelA-Diffusion and RelA-Diffusion-Latent for TAU-, PBR-, and PIB-PET generation on NFL-LONG. Inference time is measured in seconds per 3D volume.

Method	Synthesized TAU-PET Image			Synthesized PBR-PET Image			Synthesized PIB-PET Image			Inference Time \downarrow
	PSNR \uparrow	SSIM \uparrow	MAE \downarrow	PSNR \uparrow	SSIM \uparrow	MAE \downarrow	PSNR \uparrow	SSIM \uparrow	MAE \downarrow	
RelA-Diffusion	28.314 \pm 3.392	0.898 \pm 0.017	0.017 \pm 0.009	29.324 \pm 2.437	0.898 \pm 0.017	0.015 \pm 0.006	26.270 \pm 1.687	0.861 \pm 0.012	0.020 \pm 0.006	126.778
RelA-Diffusion-Latent	27.921 \pm 3.902	0.900 \pm 0.022	0.019 \pm 0.011	28.823 \pm 1.395	0.901 \pm 0.012	0.015 \pm 0.004	24.523 \pm 2.076	0.865 \pm 0.010	0.024 \pm 0.005	0.778

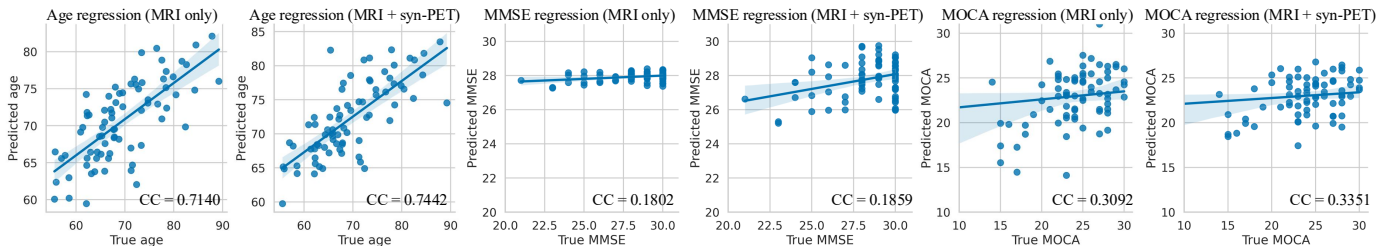


Fig. 5. Downstream regression performance for age, MMSE, and MoCA prediction using synthesized PET (syn-PET) generated from ADNI TAU images together with MRI, in comparison with MRI-only inputs.

discards T1w input. All variants retain the same network architecture as the full model. The quantitative results are reported in Table 3.

Results in Table 3 demonstrate that removing gradient penalty (GP) leads to the largest performance drop across all tracers, confirming that GP is essential for stabilizing adversarial training and preventing degradation in diffusion-GAN synthesis. Replacing the relativistic adversarial loss (RA) with a standard GAN loss also reduces fidelity, indicating that RA further enhances structural consistency. When both replacing RA with a standard GAN loss and removing GP (w/oRAGP), there is a consistent drop in PSNR and increased MAE across all tracer types, demonstrating that GP and RA are complementary, and their combination is critical for achieving high-quality PET synthesis. Excluding T1w input (w/oT1w) degrades performance, particularly for TAU- and PBR-PET, indicating that the complementary anatomical context captured by T2F and T1w MRIs is critical for accurate tracer distribution modeling. Similarly, removing T2F (w/oT2F) also causes a performance drop, but the effect is slightly less pronounced than w/oT1w, suggesting that while both modalities contribute valuable information, T1w may offer more specific pathological contrast for PET synthesis. Leveraging both T1w and T2F MRIs with relativistic adversarial supervision, the full model achieves the best performance across all three PET tracers.

5.4 Limitation and Future Work

Despite the promising results, this study has several limitations. *On one hand*, while we evaluated generalizability on ADNI, the extent to which the model is affected by domain shifts, such as variations in PET image characteristics (e.g., noise levels and spatial resolution) caused by different reconstruction algorithms, remains to be fully explored. Future work will investigate unsupervised domain adaptation [32] to enhance robustness across diverse clinical sites. *On the other hand*, the iterative nature of voxel-space diffusion models results in high computational costs. We

aim to explore diffusion distillation techniques to accelerate inference.

6 CONCLUSION

This paper presents RelA-Diffusion, a novel relativistic adversarial diffusion framework for synthesizing multi-tracer PET images from multi-sequence MRI. By leveraging T1w and T2F MRI inputs, our method captures complementary structural and pathological cues to guide the generation process. The proposed gradient-penalized relativistic adversarial loss enhances anatomical realism and stabilizes training. Extensive experiments demonstrate that RelA-Diffusion achieves superior performance in visual fidelity and quantitative accuracy compared to existing state-of-the-art methods.

REFERENCES

- [1] K. A. Johnson, A. Schultz, R. A. Betensky, J. A. Becker, J. Sepulcre, D. Rentz, E. Mormino, J. Chhatwal, R. Amariglio, K. Papp *et al.*, "Tau positron emission tomographic imaging in aging and early Alzheimer disease," *Annals of neurology*, vol. 79, no. 1, pp. 110–119, 2016.
- [2] A. J. Schwarz, P. Yu, B. B. Miller, S. Shcherbinin, J. Dickson, M. Navitsky, A. D. Joshi, M. D. Devous Sr, and M. S. Mintun, "Regional profiles of the candidate tau PET ligand 18 F-AV-1451 recapitulate key features of Braak histopathological stages," *Brain*, vol. 139, no. 5, pp. 1539–1550, 2016.
- [3] G. Antoni, M. Lubberink, S. Estrada, J. Axelsson, K. Carlson, L. Lindsjö, T. Kero, B. Långström, S.-O. Granstam, S. Rosengren *et al.*, "In vivo visualization of amyloid deposits in the heart with 11C-PIB and PET," *Journal of Nuclear Medicine*, vol. 54, no. 2, pp. 213–220, 2013.
- [4] C.-F. Xia, J. Arteaga, G. Chen, U. Gangadharmath, L. F. Gomez, D. Kasi, C. Lam, Q. Liang, C. Liu, V. P. Mocharla *et al.*, "[18F] T807, a novel tau positron emission tomography imaging agent for Alzheimer's disease," *Alzheimer's & Dementia*, vol. 9, no. 6, pp. 666–676, 2013.
- [5] A. Colasanti, Q. Guo, N. Muhlert, P. Giannetti, M. Onega, R. D. Newbould, O. Ciccarelli, S. Rison, C. Thomas, R. Nicholas *et al.*, "In vivo assessment of brain white matter inflammation in multiple sclerosis with 18F-PBR111 PET," *Journal of Nuclear Medicine*, vol. 55, no. 7, pp. 1112–1118, 2014.
- [6] W. Wei, E. Poirion, B. Bodini, M. Tonietto, S. Durrleman, O. Colliot, B. Stankoff, and N. Ayache, "Predicting PET-derived myelin content from multisequence MRI for individual longitudinal analysis in multiple sclerosis," *NeuroImage*, vol. 223, p. 117308, 2020.

- [7] S. Hu, B. Lei, S. Wang, Y. Wang, Z. Feng, and Y. Shen, "Bidirectional mapping generative adversarial networks for brain MR to PET synthesis," *IEEE Transactions on Medical Imaging*, vol. 41, no. 1, pp. 145–157, 2021.
- [8] Y. Pan, M. Liu, Y. Xia, and D. Shen, "Disease-image-specific learning for diagnosis-oriented neuroimage synthesis with incomplete multi-modality data," *IEEE Transactions on Pattern Analysis and Machine Intelligence*, vol. 44, no. 10, pp. 6839–6853, 2021.
- [9] J. Zhang, X. He, L. Qing, F. Gao, and B. Wang, "BPGAN: Brain PET synthesis from MRI using generative adversarial network for multi-modal Alzheimer's disease diagnosis," *Computer Methods and Programs in Biomedicine*, vol. 217, p. 106676, 2022.
- [10] B. Zhou, R. Wang, M.-K. Chen, A. P. Mecca, R. S. O'Dell, C. H. Van Dyck, R. E. Carson, J. S. Duncan, and C. Liu, "Synthesizing multi-tracer PET images for Alzheimer's disease patients using a 3D unified anatomy-aware cyclic adversarial network," in *International Conference on Medical Image Computing and Computer Assisted Intervention*. Springer, 2021, pp. 34–43.
- [11] Y. Pan, M. Liu, C. Lian, T. Zhou, Y. Xia, and D. Shen, "Synthesizing missing PET from MRI with cycle-consistent generative adversarial networks for Alzheimer's disease diagnosis," in *International conference on medical image computing and computer-assisted intervention*. Springer, 2018, pp. 455–463.
- [12] T. Xie, C. Cao, Z.-x. Cui, Y. Guo, C. Wu, X. Wang, Q. Li, Z. Hu, T. Sun, Z. Sang *et al.*, "Synthesizing PET images from high-field and ultra-high-field MR images using joint diffusion attention model," *Medical Physics*, vol. 51, no. 8, pp. 5250–5269, 2024.
- [13] M. Yu, M. Wu, L. Yue, A. Bozoki, and M. Liu, "Functional imaging constrained diffusion for brain PET synthesis from structural MRI," *arXiv preprint arXiv:2405.02504*, 2024.
- [14] W. Zhong, C. Cong, G. Azemi, M. Tabassum, A. Di Ieva, and S. Liu, "Multi-sequence MRI to multi-tracer PET generation via diffusion model," in *International Symposium on Biomedical Imaging*. IEEE, 2025, pp. 1–4.
- [15] I. Goodfellow, "NIPS 2016 Tutorial: Generative adversarial networks," *arXiv preprint arXiv:1701.00160*, 2016.
- [16] Z. Xiao, K. Kreis, and A. Vahdat, "Tackling the generative learning trilemma with denoising diffusion GANs," *arXiv preprint arXiv:2112.07804*, 2021.
- [17] Z. Wang, H. Zheng, P. He, W. Chen, and M. Zhou, "Diffusion-GAN: Training GANs with diffusion," in *The Eleventh International Conference on Learning Representations*, 2023.
- [18] J. Ho, A. Jain, and P. Abbeel, "Denoising diffusion probabilistic models," *Advances in Neural Information Processing Systems*, vol. 33, pp. 6840–6851, 2020.
- [19] T. Hang, S. Gu, C. Li, J. Bao, D. Chen, H. Hu, X. Geng, and B. Guo, "Efficient diffusion training via min-SNR weighting strategy," in *Proceedings of the IEEE/CVF International Conference on Computer Vision*, 2023, pp. 7441–7451.
- [20] A. Jolicœur-Martineau, "The relativistic discriminator: A key element missing from standard GAN," in *International Conference on Learning Representations*, 2019.
- [21] N. Huang, A. Gokaslan, V. Kuleshov, and J. Tompkin, "The GAN is dead; Long live the GAN! A modern gan baseline," *Advances in Neural Information Processing Systems*, vol. 37, pp. 44 177–44 215, 2024.
- [22] S. Nowozin, B. Cseke, and R. Tomioka, "f-GAN: Training generative neural samplers using variational divergence minimization," *Advances in Neural Information Processing Systems*, vol. 29, 2016.
- [23] V. Nagarajan and J. Z. Kolter, "Gradient descent GAN optimization is locally stable," *Advances in neural information processing systems*, vol. 30, 2017.
- [24] T.-C. Wang, M.-Y. Liu, J.-Y. Zhu, A. Tao, J. Kautz, and B. Catanzaro, "High-resolution image synthesis and semantic manipulation with conditional GANs," in *Proceedings of the IEEE conference on computer vision and pattern recognition*, 2018, pp. 8798–8807.
- [25] M. J. Cardoso, W. Li, R. Brown, N. Ma, E. Kerfoot, Y. Wang, B. Murrey, A. Myronenko, C. Zhao, D. Yang *et al.*, "MONAI: An open-source framework for deep learning in healthcare," *arXiv preprint arXiv:2211.02701*, 2022.
- [26] R. Rombach, A. Blattmann, D. Lorenz, P. Esser, and B. Ommer, "High-resolution image synthesis with latent diffusion models," in *Proceedings of the IEEE/CVF Conference on Computer Vision and Pattern Recognition*, 2022, pp. 10 684–10 695.
- [27] F. Bezaee, C. Desrosiers, G. A. Lodygensky, and J. Dolz, "Harmonizing Flows: Unsupervised MR harmonization based on normalizing flows," in *International Conference on Information Processing in Medical Imaging*. Springer, 2023, pp. 347–359.
- [28] S. R. Walton, Z. Y. Kerr, R. Mannix, B. L. Brett, A. Chandran, J. D. DeFreese, M. A. McCrea, K. M. Guskiewicz, W. P. Meehan, and R. J. Echemendia, "Subjective concerns regarding the effects of sport-related concussion on long-term brain health among former NFL players: An NFL-LONG study," *Sports Medicine*, pp. 1–15, 2022.
- [29] C. R. Jack Jr., M. A. Bernstein, N. C. Fox, P. Thompson, G. Alexander, D. Harvey, B. Borowski, P. J. Britson, J. L. Whitwell, C. Ward, A. M. Dale *et al.*, "The Alzheimer's disease neuroimaging initiative (ADNI): MRI methods," *Journal of Magnetic Resonance Imaging: An Official Journal of the International Society for Magnetic Resonance in Medicine*, vol. 27, no. 4, pp. 685–691, 2008.
- [30] V. L. Villemagne, A. Leuzy, S. S. Bohorquez, S. Bullich, H. Shimada, C. C. Rowe, P. Bourgeat, B. Lopresti, K. Huang, N. Krishnadas *et al.*, "CenTauR: Toward a universal scale and masks for standardizing tau imaging studies," *Alzheimer's & Dementia: Diagnosis, Assessment & Disease Monitoring*, vol. 15, no. 3, p. e12454, 2023.
- [31] K. He, X. Zhang, S. Ren, and J. Sun, "Deep residual learning for image recognition," in *Proceedings of the IEEE Conference on Computer Vision and Pattern Recognition*, 2016, pp. 770–778.
- [32] Y. Ganin and V. Lempitsky, "Unsupervised domain adaptation by backpropagation," in *International Conference on Machine Learning*. PMLR, 2015, pp. 1180–1189.